



HAL
open science

Polarizable Continuum Model based on the Solvent Excluded Surface

Chaoyu Quan, Benjamin Stamm, Yvon Maday

► **To cite this version:**

Chaoyu Quan, Benjamin Stamm, Yvon Maday. Polarizable Continuum Model based on the Solvent Excluded Surface. 2017. hal-01489262v1

HAL Id: hal-01489262

<https://hal.science/hal-01489262v1>

Preprint submitted on 14 Mar 2017 (v1), last revised 26 Feb 2018 (v2)

HAL is a multi-disciplinary open access archive for the deposit and dissemination of scientific research documents, whether they are published or not. The documents may come from teaching and research institutions in France or abroad, or from public or private research centers.

L'archive ouverte pluridisciplinaire **HAL**, est destinée au dépôt et à la diffusion de documents scientifiques de niveau recherche, publiés ou non, émanant des établissements d'enseignement et de recherche français ou étrangers, des laboratoires publics ou privés.

Polarizable Continuum Model based on the Solvent Excluded Surface

Chaoyu Quan¹, Benjamin Stamm ^{*2,3}, and Yvon Maday^{1,4,5}

¹Sorbonne Universités, UPMC Univ Paris 06, UMR 7598, Laboratoire Jacques-Louis Lions, F-75005, Paris, France (quan@ann.jussieu.fr, maday@ann.jussieu.fr)

²Center for Computational Engineering Science, RWTH Aachen University, Aachen, Germany (best@mathcces.rwth-aachen.de)

³Computational Biomedicine, Institute for Advanced Simulation IAS-5 and Institute of Neuroscience and Medicine INM-9, Forschungszentrum Jülich, Germany

⁴Institut Universitaire de France, 75005, Paris, France

⁵Division of Applied Mathematics, Brown University, 182 George St, Providence, RI 02912, USA

Abstract

In this article, we introduce a new Polarizable Continuum Model (PCM) based on the Solvent Excluded Surface (SES). The model incorporates an intermediate switching region for the solute-solvent dielectric boundary to enhance a smooth electrostatic contribution to the solvation energy. The Schwarz domain decomposition method is applied to solve this model, the crucial part of which is the discretization of each local equation defined on a subdomain (consisting of a ball) based on the spherical harmonics in the angular direction and the Legendre polynomials in the radial direction. A series of numerical tests are presented to show the performance of the proposed method for this model.

Keywords: Polarizable continuum model; Solvent excluded surface; Solvation energy; Domain decomposition method

1 Introduction

Most of the physical and chemical phenomena of interest in chemistry and biology take place in the liquid phase, and it is well known that solvent effects play a crucial role in these processes. There are basically two different approaches to account for solvent effects in the computation of the properties of a solvated molecule or ion. The first approach is to use an explicit solvent model, in which the simulated chemical system is composed of the solute molecule and of a large number of solvent molecules. The second approach is to use an implicit solvent model, in which the solute molecule under study, sometimes together with a small number of solvent molecules weakly bonded to the solute, is embedded in a cavity surrounded by a continuous medium modeling the solvent. Implicit solvent models are widely used in practice and the Polarizable Continuum Model (PCM)

*Preprint to Mathematical Models and Methods in Applied Sciences.

is a popular type of implicit solvent model which represents the solvent as a polarizable continuum. For the sake of brevity, we will not elaborate here on their capabilities and limitations, nor on their applications in chemistry and bio-chemistry, and refer the reader to the monograph and the review articles [2, 32, 19] and references therein.

1.1 Previous works

An integral equation formalism (IEF) [5, 20, 4] of the PCM was first proposed by E Cancès, B Mennucci and J Tomasi, which has been the default PCM formulation in Gaussian [7]. From the computational point of view, one big advantage of this formalism is that it transforms the original problem defined in the 3D space equivalently to an integral equation on the dielectric boundary and therefore the computational cost can be greatly reduced. Another popular implicit solvent model is the conductor-like screening model (COSMO) [13] where the solvent is modeled as a conductor-like continuum. This model can be seen as a special case of the PCM where the solvent dielectric constant is set to $+\infty$ and the solvent is therefore represented by a perfect conductor.

In the passed several years, a new algorithm for solving the COSMO has been developed using the domain decomposition method, called the ddCOSMO method [3, 18, 15, 17]. This algorithm has attracted much attention because of its very impressive efficiency, that is, it performs up to two orders of magnitude faster than the algorithm in Gaussian [15]. Recently, a similar discretization for the PCM within the domain decomposition paradigm was proposed, called the ddPCM method [31], which is based on the IEF-PCM. One important fact is that both the ddCOSMO and the ddPCM work only for the solute cavity constituted by the union of balls, such as the van der Waals (VdW) cavity and the Solvent Accessible Surface cavity (SAS-cavity) [14, 29]. Due to the recent progress, the resolution of the COSMO and the PCM by ddCOSMO resp. ddPCM has become sufficiently fast (see website [16]) so that one start to raise the question of the proper definition of the solute cavity.

Indeed, the choice of the cavity is important as pointed out in [33, Section II. C.]: *The shape and size of the cavity are critical factors in the elaboration of a method. An ideal cavity should reproduce the shape of the solute M , with the inclusion of the whole charge distribution ρ_M and with the exclusion of empty spaces which can be filled by the solvent continuous distribution.*

Besides the VdW-cavity and the SAS-cavity, there is another well-known solute cavity, called the Solvent Excluded Surface cavity (SES-cavity), associated with the Solvent Excluded Surface (SES) which is the so-called “smooth” molecular surface. The SES-cavity has a stronger physical meaning than the SAS-cavity in the sense that the SES-cavity takes the size of solvent molecules better into account and represents better the region where the solvent molecules have no access in the spirit of the quote above. This suggests that taking the SES-cavity into account might yield more accurate results than with the SAS-cavity which is confirmed so far in [28, 23]. Moreover, in a recent work [24, 25] of some of us, we have presented a complete characterization of the SES including all possible SES-singularities, which were not characterized completely until then. This allows us to further generalize the ddCOSMO and the ddPCM from the VdW-cavity or the SAS-cavity to the SES-cavity. The topology of the SES-cavity is much more challenging with respect to the VdW-cavity or the SAS-cavity which consists of the topological boundary of overlapping spheres.

1.2 Contribution

In this article, we propose a new PCM based on the SES, where an intermediate region for the solute-solvent dielectric boundary is constructed and the dielectric permittivity varies smoothly from the SES-cavity to the solvent region. The corresponding dielectric permittivity function is a distance-dependent (to the SES) continuous function associated with the signed distance function to the Solvent Accessible Surface (SAS), which is used to implicitly define the SES. To solve the electrostatic problem of this new model, a global strategy is consequently proposed, in which we use the domain decomposition method involving only local problems in a ball. We develop a solver suited to the Generalized Poisson (GP) equation defined in each ball. We also present some numerical results to illustrate the performance of this method for the proposed PCM.

To our knowledge, this is the first time that a continuous dielectric permittivity function of the PCM is constructed based on the exact SES-cavity since the complete characterization of the SES has just been finished [24, 25]. In addition, we provide a new domain decomposition method that implicitly relies on integral equations but explicitly only requires to solve Partial Differential Equations (PDEs) on bounded sub-domains.

1.3 Outline

In Section 2, we first introduce different solute cavities including the VdW-cavity, the SAS-cavity and the SES-cavity. Then, in Section 3, we propose a new PCM based on the SES-cavity by constructing a continuous permittivity function associated with the signed distance to the SAS, which ensures that the SES-cavity always has the permittivity of vacuum. Next, we present the formulation of the electrostatic problem for this new PCM and the global strategy for solving it in Section 4. In Section 5, we introduce the domain decomposition scheme for solving iteratively the partial differential equations in the global strategy. This domain decomposition method requires to develop a Laplace solver and a GP-solver for the unit ball, which are presented in Section 6. After that, in Section 7, we illustrate a series of numerical results about computing the electrostatic contribution to the solvation energy of the new PCM based on the SES-cavity. In the last section, we draw some conclusions.

2 Solute cavities

In an implicit solvent model, the solvent is represented as a continuous medium instead of individual explicit solvent molecules. In this case, it is important to choose a suitable solute-solvent boundary, the interface between the solute cavity and the solvent cavity, which is an important ingredient of the model. One choice of the solute cavity is the VdW-cavity which is the union of solute VdW-atoms with radii experimentally fitted given the underlying chemical element, for example the UFF-radii [27].

Another choice is to model the solute surface taking the solvent molecules into account and consequently model the solute cavity as the region enclosed by this surface. The solvent accessible surface is such a solute surface defined by rolling the center of an idealized spherical probe (representing a solvent molecule) over a solute molecule. The surface enclosing the region in which the center of this spherical probe can not enter builds the SAS. In consequence, the region enclosed by the SAS is called the SAS-cavity, denoted by Ω_{sas} . Besides, another model for the solute surface has been established, the solvent excluded surface. The SES is defined by the same spherical probe

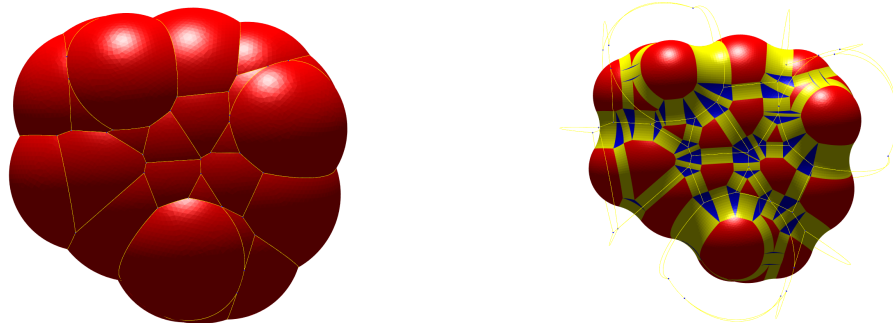


Figure 1: The SAS (left, Γ_{sas}) and the SES (right, Γ_{ses}) of caffeine with solvent probe radius $r_p = 1.5\text{\AA}$. On the right, the SES is composed of convex spherical patches (red), toroidal patches (yellow) and concave spherical patches (blue).

rolling over the solute molecule, but considering now the surface enclosing the region in which the spherical probe itself (not its center) can not access. Similarly, this region enclosed by the SES is called the SES-cavity, denoted by Ω_{ses} . In other words, the SES is the boundary of the union of all spherical probes that do not intersect the VdW-balls (with scale factor 1) of the solute molecule.

Figure 1 gives a graphical illustration of the SAS and the SES of caffeine derived from our recent work [24]. From the geometrical point of view, the SES is smoother than the VdW-surface or the SAS and furthermore, the SES-cavity has a strong physical meaning that it is the cavity where the (idealized) solvent molecules can not touch because of the presence of the solute. It is actually implicitly assumed that the solvent molecule can not overlap any VdW-atom of the solute.

To set the notation, we suppose that the solute molecule is composed of M atoms and the j th atom has a center \mathbf{c}_j and a radius r_j . The probe radius is denoted by r_p . For each $1 \leq j \leq M$, we define an “enlarged” ball Ω_j with center \mathbf{c}_j and radius $R_j = r_j + r_p + r_0$ where r_0 is some nonnegative constant. In the following content, we assume that the solvent dielectric constant (also called permittivity) outside the union of these “enlarged” balls is a constant ϵ_s . This assumption is reasonable in the sense that the solvent density at positions far from the solute molecule (bulk) is approximately the same. Therefore, the dielectric permittivity determined by the solvent density is assumed to be constant [8, 1].

Thus, the solute molecule should be completely contained in the union of these enlarged balls. We denote the union of these balls Ω_j by

$$\Omega_0 = \bigcup_{j=1}^M \Omega_j, \quad \text{with} \quad \Omega_j = B_{R_j}(\mathbf{c}_j).$$

In addition, we denote the boundary surfaces associated with the above-mentioned cavities as $\Gamma_{\text{sas}} = \partial\Omega_{\text{sas}}$, $\Gamma_{\text{ses}} = \partial\Omega_{\text{ses}}$, $\Gamma_0 = \partial\Omega_0$.

Denoting by f_{sas} the signed distance function to the SAS (negative inside the SAS and positive outside the SAS), we have consequently a mathematical characterization of the three cavities: $\Omega_{\text{sas}} = \{\mathbf{p} \in \mathbb{R}^3 : f_{\text{sas}}(\mathbf{p}) \leq 0\}$, $\Omega_{\text{ses}} = \{\mathbf{p} \in \mathbb{R}^3 : f_{\text{sas}}(\mathbf{p}) \leq -r_p\}$ and $\Omega_0 = \{\mathbf{p} \in \mathbb{R}^3 : f_{\text{sas}}(\mathbf{p}) \leq r_0\}$ and also a characterization of the three boundary surfaces: $\Gamma_{\text{sas}} = f_{\text{sas}}^{-1}(0)$, $\Gamma_{\text{ses}} = f_{\text{sas}}^{-1}(-r_p)$ and $\Gamma_0 = f_{\text{sas}}^{-1}(r_0)$. In our recent work [24], we have presented a direct and efficient way to compute

analytically the function value of f_{sas} based on finding the closest point on the SAS to an arbitrary point and consequently a complete characterization of the SES including all singularities. This allows us to propose in the next section a new PCM based on the SES-cavity with its permittivity function associated through f_{sas} .

3 Continuous Permittivity function

In the classical PCM based on some solute cavity Ω [21], the permittivity ϵ is defined as

$$\epsilon = \begin{cases} 1 & \text{in } \Omega, \\ \epsilon_s & \text{in } \mathbb{R}^3 \setminus \Omega, \end{cases} \quad (3.1)$$

which implies that there is a jump of the permittivity on the cavity boundary $\partial\Omega$. This solute cavity is usually taken to be formed by overlapping spheres, for example, the VdW-cavity and the SAS-cavity. However, both the VdW-cavity and the SAS-cavity can have topological issues. For instance, they can present holes that allow the solvent to penetrate in nonphysical regions. As a first remedy, the scaled VdW-radii is usually used, in the model of which each atom has a radius equal to its corresponding VdW-radii multiplied by an empirical factor $1.1 \sim 1.2$, see the discussion in [33, Section II. C.]. However, this might increase the volume of the solute too much so that solvent can not access in regions it should. From [33] we quote: *If the cavity is too large the solvation effects are damped; if it is too small serious errors may arise in the evaluation of the interaction energy for the portions of ρ_M (atoms or bonds) near the boundaries.* The problem is that the VdW- and SAS-cavities are topologically not the correct answer to the problem and scaling the radius is only partially satisfying. The SES-cavity, which is topologically more involved than the VdW-cavity or the SAS-cavity, provides a remedy since it is topologically more accurate as motivated in the introduction.

In this article, we propose another PCM taking into account the SES-cavity to compute the electrostatic contribution to the solvation energy. We treat the SES as the solute-solvent dielectric boundary (or the solute cavity boundary) meaning that the dielectric permittivity in the SES-cavity is always one, i.e., the permittivity of vacuum. Furthermore, we assume that the permittivity varies smoothly in an intermediate switching region between Γ_{ses} and Γ_0 , called the dielectric boundary layer, see the left of Figure 2 for a 2D schematic diagram. Outside the cavity Ω_0 , the permittivity is taken to be the solvent dielectric constant ϵ_s as assumed in Section 2.

The crucial part is to determine the way the permittivity changes from 1 to ϵ_s . To our knowledge, the dielectric permittivity is greatly affected by the solvent density which has a fluctuation behavior (see [6] and Chapter 1 of [11]) near the solute due to solvent ordering. This implies that it is not sufficient to take a constant value for modeling the solvent environment. Many attempts have been done to introduce a continuous change of dielectric permittivity occurring near the solute cavity [12, 8, 1]. However, in these models, the permittivity function are usually based on the VdW-cavity (or VdW-atoms) and the permittivity value can only be ensured to be one in the VdW-cavity but not in the SES-cavity. To construct a intuitively more physical permittivity model which ensures that the SES-cavity (i.e. the region where the solvent can not access) completely has the permittivity of vacuum, we propose a continuous permittivity function which depends on the signed distance function f_{sas} to the SAS. Precisely speaking, we give a definition of the permittivity function ϵ in

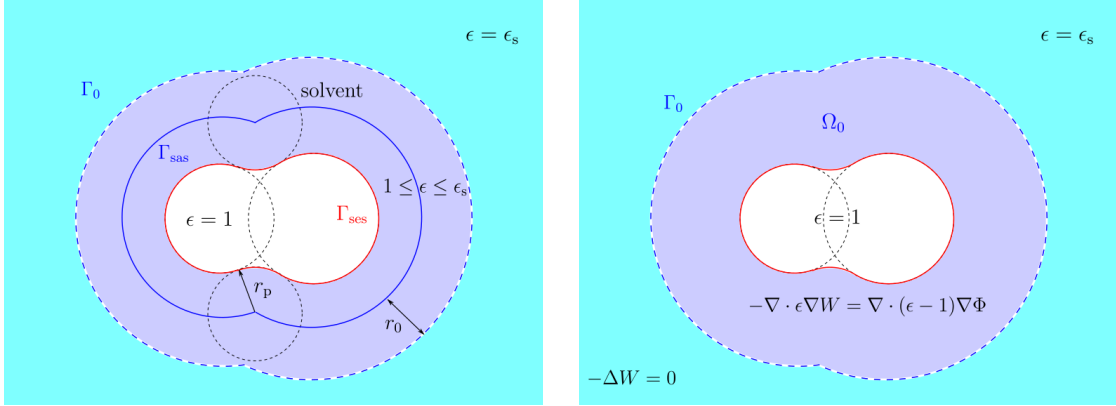


Figure 2: 2D schematic diagrams of the permittivity function ϵ (left) and the electrostatic problem (right) for a two atomic system. The permittivity ϵ in the dielectric boundary layer (dark blue region) between two interfaces Γ_{ses} (red curve) and Γ_0 (dashed blue curve) varies smoothly from 1 inside Γ_{ses} to ϵ_s outside Γ_0 .

the form of

$$\epsilon(\mathbf{p}) = \begin{cases} 1 & \mathbf{p} \in \Omega_{ses}, \\ H\left(\frac{f_{sas}(\mathbf{p}) + r_p}{r_p + r_0}\right) & \mathbf{p} \in \Omega_0 \setminus \Omega_{ses}, \\ \epsilon_s & \mathbf{p} \in \Omega_0^c, \end{cases} \quad (3.2)$$

where $\Omega_0^c = \mathbb{R}^3 \setminus \Omega_0$ and H is a continuous function defined on $[0, 1]$ satisfying $H(0) = 1$, $H(1) = \epsilon_s$. Note that ϵ is ensured to be continuous in the whole 3D space, especially on the boundary Γ_{ses} and Γ_0 . Moreover, ϵ can be seen as a distance-dependent function where the “distance” represents the signed distance to the SAS. See Figure 3 for a schematic diagram of the dielectric permittivity function.

To guarantee the smoothness of permittivity on two interfaces Γ_{ses} and Γ_0 , we can impose more conditions to the function H , for example,

$$H'(0) = 0, \quad H'(1) = 0, \quad H''(0) = 0, \quad H''(1) = 0.$$

In this case, ϵ is twice continuously differentiable almost everywhere on Γ_{ses} and Γ_0 since f_{sas} is twice continuously differentiable almost everywhere. In the following content, we simply choose a S-shaped polynomial function as H for numerically computing the electrostatic contribution to the solvation energy:

$$H(t) = 1 + (\epsilon_s - 1)t^3(10 + 3t(-5 + 2t)), \quad 0 \leq t \leq 1. \quad (3.3)$$

With the above function H , the jump of the normal derivative of the permittivity function is zero on the boundary Γ_{ses} and Γ_0 .

Remark 3.1. *We emphasize that the function H can be chosen in many different manners satisfying various conditions. This characterizes the way the permittivity varies in the intermediate switching region. The definition (3.3) of H is the version that we considered in the numerical tests of the proposed algorithm.*

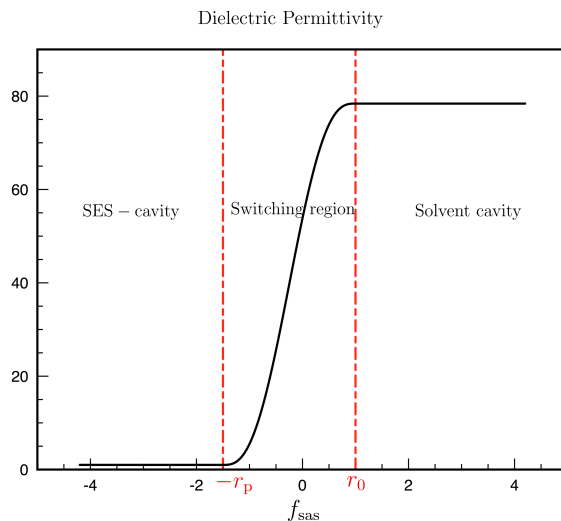


Figure 3: 2D schematic diagram of the dielectric permittivity function with respect to f_{sas} . The switching region (dielectric boundary layer) is bounded by two dashed lines (red), i.e., the region where $-r_p \leq f_{\text{sas}} \leq r_0$.

We mention that the above-proposed model can also be used to approach classical polarizable continuum models with sharp interfaces. If one chooses a sequence of H approaching the following discontinuous function

$$\chi_1(t) = \begin{cases} 1 & t < -r_p, \\ \epsilon_s & t \geq -r_p, \end{cases} \quad (3.4)$$

then the governing equations of the above-proposed PCM approaches the equations of a PCM where the SES-cavity is in vacuum and is surrounded by the continuum medium, i.e. with a sharp interface between solvent and solute. Similarly, if H approaches the following discontinuous function

$$\chi_2(t) = \begin{cases} 1 & t < 0, \\ \epsilon_s & t \geq 0, \end{cases} \quad (3.5)$$

then the governing equations of the above-proposed PCM approaches the equations of the PCM based on the SAS-cavity where the SAS-cavity is in vacuum and is surrounded by the continuum medium.

4 Problem formulation and global strategy

4.1 Problem formulation

With the above PCM based on the SES-cavity, we aim to compute the electrostatic contribution to the solvation energy, denoted by E^s . This contribution E^s can be written as

$$E^s = \frac{1}{2} \int_{\mathbb{R}^3} \rho(\mathbf{r}) W(\mathbf{r}) d\mathbf{r}, \quad (4.6)$$

where W denotes the (solvent) reaction potential generated by the solute's charge density ρ in presence of the dielectric continuum. The governing equations for the potential W will be explained in this section.

We postpone the definition of W and assume that the electrostatic potential Φ generated by the solute's charge density ρ in vacuum is already known and ρ is supported in Ω_{ses} , i.e. $\text{supp}(\rho) \subset \Omega_{\text{ses}}$, which is a standard assumption in the content of the PCM. Notice that Φ satisfies the following partial differential equation (PDE)

$$-\Delta\Phi = 4\pi\rho, \quad \text{in } \mathbb{R}^3. \quad (4.7)$$

As presented in [3], we consider for simplicity a neutral solute molecule with a classical charge distribution

$$\rho(\mathbf{r}) = \sum_{j=1}^M q_j \delta_{\mathbf{c}_j}(\mathbf{r}), \quad \forall \mathbf{r} \in \mathbb{R}^3, \quad (4.8)$$

where q_j represents the charge of the j th atom and $\delta_{\mathbf{c}_j}$ is the Dirac function at the atomic center \mathbf{c}_j . In consequence, the electrostatic potential Φ generated by ρ is derived as

$$\Phi(\mathbf{r}) = \sum_{j=1}^M \frac{q_j}{|\mathbf{r} - \mathbf{c}_j|}. \quad (4.9)$$

In the PCM, the electrostatic potential V generated by the solute's charge density ρ satisfies the following PDE

$$-\nabla \cdot \epsilon \nabla V = 4\pi\rho, \quad \text{in } \mathbb{R}^3 \quad (4.10)$$

and $V(\mathbf{r}) \sim \frac{1}{|\mathbf{r}|}$ as $|\mathbf{r}| \rightarrow \infty$.

The reaction potential W , defined by $W = V - \Phi$, is the difference between the electrostatic potentials with and without the presence of the implicit solvent which satisfies

$$\begin{cases} \Delta W = 0 & \text{in } \Omega_{\text{ses}}, \\ -\nabla \cdot \epsilon \nabla W = \nabla \cdot \epsilon \nabla \Phi & \text{in } \Omega_0 \setminus \Omega_{\text{ses}}, \\ \Delta W = 0 & \text{in } \Omega_0^c, \end{cases} \quad (4.11)$$

where $\Omega_0^c = \mathbb{R}^3 \setminus \Omega_0$. Further, at the interfaces Γ_{ses} and Γ_0 , we require the following classical jump-conditions

$$\begin{cases} [W] = 0 & \text{on } \Gamma_{\text{ses}} \text{ and } \Gamma_0, \\ [\partial_{\mathbf{n}_0} W] = 0 & \text{on } \Gamma_{\text{ses}} \text{ and } \Gamma_0, \end{cases} \quad (4.12)$$

since the permittivity ϵ is continuous across the interfaces. Here, \mathbf{n}_0 is the unit normal vector on Γ_0 pointing outwards with respect to Ω_0 , $\partial_{\mathbf{n}_0} W$ denotes the normal derivative $\nabla W \cdot \mathbf{n}_0$, $[W]$ denotes the jump (inside minus outside) of the reaction potential W on the boundary surfaces Γ_{ses} and Γ_0 , $[\partial_{\mathbf{n}_0} W]$ denotes the jump of the normal derivative of the reaction potential. Since $\text{supp}(\rho) \subset \Omega_{\text{ses}}$ and $\epsilon = 1$ in Ω_{ses} , we have $\Delta\Phi = 0$ in $\Omega_0 \setminus \Omega_{\text{ses}}$ and consequently the above Eqs (4.11)–(4.12) can be recast as

$$\begin{cases} -\nabla \cdot \epsilon \nabla W = \nabla \cdot (\epsilon - 1) \nabla \Phi & \text{in } \Omega_0, \\ \Delta W = 0 & \text{in } \Omega_0^c, \end{cases} \quad (4.13)$$

in combination with

$$\begin{cases} [W] = 0 & \text{on } \Gamma_0, \\ [\partial_{\mathbf{n}_0} W] = 0 & \text{on } \Gamma_0. \end{cases} \quad (4.14)$$

See the right of Figure 2 for a 2D schematic diagram.

In the second equation of (4.13), a single layer potential $\widetilde{\mathcal{S}}_{\Gamma_0} : H^{-\frac{1}{2}}(\Gamma_0) \rightarrow H^1(\Omega_0^c)$ can be used to represent the electrostatic potential W restricted in Ω_0^c as follows

$$(\widetilde{\mathcal{S}}_{\Gamma_0} \sigma)(\mathbf{r}) = \int_{\Gamma_0} \frac{\sigma(\mathbf{s}')}{|\mathbf{r} - \mathbf{s}'|} d\mathbf{s}' = W|_{\Omega_0^c}(\mathbf{r}), \quad \forall \mathbf{r} \in \Omega_0^c, \quad (4.15)$$

where σ is some function in $H^{-\frac{1}{2}}(\Gamma_0)$. From the continuity of the single-layer potential across the interface, see for example [30, 9], we take the limit to Γ_0 , so as to obtain the integral equation

$$(\mathcal{S}_{\Gamma_0} \sigma)(\mathbf{s}) = \int_{\Gamma_0} \frac{\sigma(\mathbf{s}')}{|\mathbf{s} - \mathbf{s}'|} d\mathbf{s}' = W|_{\Gamma_0}(\mathbf{s}), \quad \forall \mathbf{s} \in \Gamma_0, \quad (4.16)$$

where $\mathcal{S}_{\Gamma_0} : H^{-\frac{1}{2}}(\Gamma_0) \rightarrow H^{\frac{1}{2}}(\Gamma_0)$ is the single-layer operator which is invertible (see also [30, 9]) and thus defines $\sigma \in H^{-\frac{1}{2}}(\Gamma_0)$. Further, we can artificially extend the potential defined by (4.15) to Ω_0 as follows

$$\widetilde{W}(\mathbf{r}) := \int_{\Gamma_0} \frac{\sigma(\mathbf{s}')}{|\mathbf{r} - \mathbf{s}'|} d\mathbf{s}', \quad \forall \mathbf{r} \in \Omega_0 \quad (4.17)$$

satisfying

$$\Delta \widetilde{W} = 0, \quad \text{in } \Omega_0 \quad (4.18)$$

and

$$\widetilde{W} = W|_{\Omega_0^c}, \quad \text{on } \Gamma_0. \quad (4.19)$$

Recalling the relationship between the charge density σ and the jump of the normal derivative of the potential on Γ_0 generated by σ [31], we actually have

$$\sigma = \frac{1}{4\pi} (\partial_{\mathbf{n}_0} \widetilde{W} - \partial_{\mathbf{n}_0} W|_{\Omega_0^c}), \quad \text{on } \Gamma_0. \quad (4.20)$$

Combining with $[\partial_{\mathbf{n}_0} W] = 0$ on Γ_0 in (4.14), i.e., $\partial_{\mathbf{n}_0} W|_{\Omega_0} = \partial_{\mathbf{n}_0} W|_{\Omega_0^c}$, we therefore obtain

$$\sigma = \frac{1}{4\pi} (\partial_{\mathbf{n}_0} \widetilde{W} - \partial_{\mathbf{n}_0} W|_{\Omega_0}), \quad \text{on } \Gamma_0. \quad (4.21)$$

Also, since $[W] = 0$ in (4.14) and $\widetilde{W} = W|_{\Omega_0^c}$ on Ω_0 , we have $\widetilde{W} = W$ on Γ_0 .

Finally, let's summary what we have in hand now. We have obtained two PDEs of W and \widetilde{W} both defined on Ω_0

$$\begin{cases} -\nabla \cdot \epsilon \nabla W = \nabla \cdot (\epsilon - 1) \nabla \Phi & \text{in } \Omega_0, \\ \Delta \widetilde{W} = 0 & \text{in } \Omega_0, \end{cases} \quad (4.22)$$

and two boundary conditions coupling them

$$\begin{cases} W = \widetilde{W} & \text{on } \Gamma_0, \\ \sigma = \frac{1}{4\pi} (\partial_{\mathbf{n}_0} \widetilde{W} - \partial_{\mathbf{n}_0} W) & \text{on } \Gamma_0, \end{cases} \quad (4.23)$$

where σ is the density generating \widetilde{W} by (4.17). To compute the electrostatic contribution to the solvation energy, we need to compute W which involves solving Eqs (4.22)–(4.23). Although we solve for a problem in an unbounded domain, we need to solve equations only on the bounded domain Ω_0 which is a remarkable property.

4.2 Global strategy

From the above formulation, we propose the following iterative procedure for solving Eqs (4.22)–(4.23): Let g^0 be an initial guess for the Dirichlet condition $W|_{\Gamma_0} = \widetilde{W}|_{\Gamma_0}$ on Γ_0 and set $k = 1$.

- [1] Solve the following Dirichlet boundary problem for W^k :

$$\begin{cases} -\nabla \cdot \epsilon \nabla W^k = \nabla \cdot (\epsilon - 1) \nabla \Phi & \text{in } \Omega_0, \\ W^k = g^{k-1} & \text{on } \Gamma_0, \end{cases} \quad (4.24)$$

and derive its Neumann boundary trace $\partial_{\mathbf{n}_0} W^k$ on Γ_0 .

- [2] Solve the following Dirichlet boundary problem for \widetilde{W}^k :

$$\begin{cases} -\Delta \widetilde{W}^k = 0 & \text{in } \Omega_0, \\ \widetilde{W}^k = g^{k-1} & \text{on } \Gamma_0, \end{cases} \quad (4.25)$$

and derive similarly its Neumann boundary trace $\partial_{\mathbf{n}_0} \widetilde{W}^k$ on Γ_0 .

- [3] Build the charge density $\sigma^k = \frac{1}{4\pi} (\partial_{\mathbf{n}_0} \widetilde{W}^k - \partial_{\mathbf{n}_0} W^k)$ and compute a new Dirichlet condition $g^k = \mathcal{S}_{\Gamma_0} \sigma^k$.
- [4] Compute the electrostatic contribution E_k^s to the solvation energy following (4.6) based on W^k at the k -th iteration, set $k \leftarrow k + 1$, go back to Step [1] and repeat until the increment of electrostatic interaction $|E_k^s - E_{k-1}^s|$ becomes smaller than a given tolerance $\text{To1} \ll 1$.

Remark 4.1. *In order to provide a suitable initial guess of g^0 , we consider the (unrealistic) scenario where the whole space \mathbb{R}^3 is covered by the solvent medium with the permittivity ϵ_s . In consequence, the electrostatic potential V is given by $V = \frac{1}{\epsilon_s} \Phi$ and the reaction potential is provided by $W = V - \Phi = \left(\frac{1}{\epsilon_s} - 1\right) \Phi$. We therefore propose the following initial Dirichlet boundary function g^0 for the first iteration:*

$$g^0 = \left(\frac{1}{\epsilon_s} - 1\right) \Phi. \quad (4.26)$$

Remark 4.2. *This iterative procedure has the remarkable property that we solve a problem on an unbounded domain by a sequence of problems on bounded domains only. It can be seen as a domain decomposition method on the two non-overlapping domains Ω_0 and Ω_0^c where only problems on the bounded domain Ω_0 are solved.*

In the next section, we propose to use the classical Schwarz domain decomposition method to solve the PDE (4.24) in Step [1] and the PDE (4.25) in Step [2] by introducing sub-iterations.

5 Domain decomposition strategy

The Schwarz's domain decomposition method [26] aims at solving partial differential equations defined on complex domains which can be decomposed as a union of overlapping and possibly simple subdomains. For each subdomain, the same equation is solved but with boundary conditions that depend on the global boundary condition on one hand and on the neighboring solutions on the other hand.

Recalling that we have a natural domain decomposition of Ω_0 as follows

$$\Omega_0 = \bigcup_{j=1}^M \Omega_j, \quad \Omega_j = B_{R_j}(\mathbf{c}_j),$$

the Schwarz's domain decomposition method can be applied to solve the PDE (4.24). We replace the global equation (4.24) by the following coupled equations, each restricted to Ω_j :

$$\begin{cases} -\nabla \cdot \epsilon \nabla W_j = \nabla \cdot (\epsilon - 1) \nabla \Phi & \text{in } \Omega_j, \\ W_j = h_j & \text{on } \Gamma_j, \end{cases} \quad (5.27)$$

where $W_j = W|_{\Omega_j}$, $\Gamma_j = \partial\Omega_j$ and

$$h_j = \begin{cases} W_j^{\mathcal{N}} & \text{on } \Gamma_j^i, \\ g & \text{on } \Gamma_j^e. \end{cases} \quad (5.28)$$

Here, we omit the superscript due to the (outer) iteration index k . Γ_j^e is the external part of Γ_j not contained in any other ball Ω_i ($i \neq j$), i.e., $\Gamma_j^e = \Gamma_0 \cap \Gamma_j$, Γ_j^i is the internal part of Γ_j , i.e., $\Gamma_j^i = \Omega_0 \cap \Gamma_j$ (see Figure 4 for an illustration), and

$$W_j^{\mathcal{N}}(\mathbf{s}) = \frac{1}{|\mathcal{N}(j, \mathbf{s})|} \sum_{i \in \mathcal{N}(j, \mathbf{s})} W_i(\mathbf{s}), \quad \forall \mathbf{s} \in \Gamma_j^i, \quad (5.29)$$

where $\mathcal{N}(j, \mathbf{s})$ represents the index set of all balls that overlap Ω_j at \mathbf{s} . In fact, for a fixed point $\mathbf{s} \in \Gamma_j^i$, we enforce $W_j = W_j^{\mathcal{N}}(\mathbf{s})$.

In the next section, we will develop a GP-solver for solving the local problems (5.27). For each local problem defined on Ω_j , this solver provides an approximate weak solution. Based on this solver, an iterative procedure can be applied to solve the coupled equations (5.27)–(5.28), such as the Jacobi or Gauss-Seidel algorithms as presented in [3]. The idea of the Jacobi algorithm is to solve each local problem based on the boundary condition of the neighboring solutions derived from the previous iteration. During this iterative procedure, the computed value of $W|_{\Gamma_j^i}$ is updated step by step and converges to the exact value.

The Jacobi or Gauss-Seidel algorithms are not the most efficient way to solve this set of equations, but is well-suited to illustrate the idea of domain decomposition. In practice, a global problem (linear system after introducing a discretization) might be solved with GMRes for example.

Remark 5.1. Notice that the global strategy for computing the electrostatic contribution to the solvation energy in Section 4.2 is also an iterative process (it was indexed by k). To distinguish these two iterations, the global iteration in Section 4.2 is called the outer iteration and the iteration of solving the GP-equation Eq. (4.24) by iteratively solving the set of local problems (5.27) is called the inner iteration. Of course, for the sake of efficiency, these two iterations (inner and outer) should be intertwined.

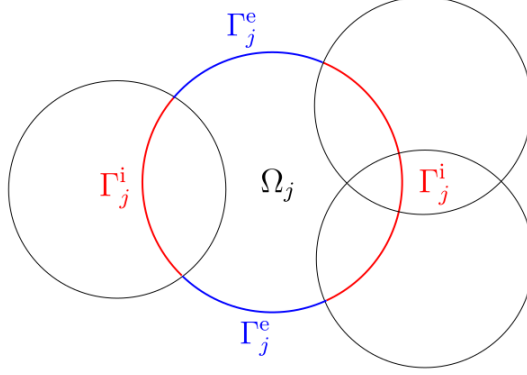


Figure 4: 2D schematic diagram of Γ_j^i (red) and Γ_j^e (blue) associated with Ω_j .

As to solve the Laplace equation (4.25), we still use the domain decomposition method which is called the ddCOSMO method in this context and has been developed in [3]. In fact, Eq. (4.25) can be seen as a special case of Eq. (4.24) when $\epsilon = 1$. In consequence, the same domain decomposition method as presented in (5.27)–(5.28) can be used where each local problem (5.27) simplifies to a Laplace problem.

6 Single-domain solvers

6.1 Laplace equation in a ball

As seen above, it is required to solve a set of coupled Laplace equations, each of which is restricted to a ball as in the ddCOSMO. For the sake of completeness, we now introduce briefly the ideas. Without loss of generality, we consider the following Laplace equation with the Dirichlet boundary condition ϕ_0 and defined in the unit ball with center $\mathbf{0}$:

$$\begin{cases} \Delta u_0 = 0 & \text{in } B_1(\mathbf{0}), \\ u_0 = \phi_0 & \text{on } \partial B_1(\mathbf{0}). \end{cases} \quad (6.30)$$

where $B_1(\mathbf{0})$ represents the unit ball centered at the origine $\mathbf{0}$. In consequence, the unique solution to (6.30) in $H^1(B_1(\mathbf{0}))$ can be written as

$$u_0(r, \theta, \varphi) = \sum_{\ell=0}^{\infty} \sum_{m=-\ell}^{\ell} [\phi_0]_{\ell}^m r^{\ell} Y_{\ell}^m(\theta, \varphi), \quad 0 \leq r \leq 1, \quad 0 \leq \theta \leq \pi, \quad 0 \leq \varphi < 2\pi, \quad (6.31)$$

where Y_{ℓ}^m is the (orthonormal) spherical harmonic of degree ℓ and order m defined on \mathbb{S}^2 and

$$[\phi_0]_{\ell}^m = \int_{\mathbb{S}^2} \phi_0(\mathbf{s}) Y_{\ell}^m(\mathbf{s}) d\mathbf{s}$$

is the real coefficient of u_0 corresponding to the mode Y_{ℓ}^m .

To compute (6.31) numerically, we first approximate $[\phi_0]_\ell^m$ using the Lebedev quadrature rule [10] defined by the integration points $\mathbf{s}_n \in \mathbb{S}^2$ and their weights w_n^{leb} as follows

$$[\tilde{\phi}_0]_\ell^m = \sum_{n=1}^{N_{\text{leb}}} w_n^{\text{leb}} \phi_0(\mathbf{s}_n),$$

where N_{leb} represents the number of Lebedev points. Then, u_0 can be approximated by \tilde{u}_0 in the discretization space spanned by a truncated basis of spherical harmonics $\{Y_\ell^m\}_{0 \leq \ell \leq \ell_{\text{max}}, -\ell \leq m \leq \ell}$, defined as

$$\tilde{u}_0(r, \theta, \varphi) = \sum_{\ell=0}^{\ell_{\text{max}}} \sum_{m=-\ell}^{\ell} [\tilde{\phi}_0]_\ell^m r^\ell Y_\ell^m(\theta, \varphi), \quad 0 \leq r \leq 1, \quad 0 \leq \theta \leq \pi, \quad 0 \leq \varphi < 2\pi \quad (6.32)$$

where ℓ_{max} denotes the maximum degree of spherical harmonics. This approximate solution \tilde{u}_0 converges to the exact solution u_0 to Eq. (6.30) when $\ell_{\text{max}} \rightarrow \infty$ and $N_{\text{leb}} \rightarrow \infty$. One should note however that there is no systematic manner to derive Lebedev points of arbitrary accuracy.

6.2 Generalized Poisson equation in a ball

To solve the local equations (5.27), we need to develop a solver for the GP-equation defined on Ω_j with the Dirichlet boundary condition (5.28). Without loss of generality, we discuss how to solve the following GP-equation in the unit ball with center $\mathbf{0}$ in the general form of

$$\begin{cases} -\nabla \cdot \epsilon_1(\mathbf{x}) \nabla u_1(\mathbf{x}) = f_1(\mathbf{x}) & \text{in } B_1(\mathbf{0}), \\ u_1(\mathbf{x}) = \phi_1(\mathbf{x}) & \text{on } \partial B_1(\mathbf{0}). \end{cases} \quad (6.33)$$

In fact, for any $j = 1, \dots, M$, we take $\epsilon_1(\mathbf{x}) = \epsilon(\mathbf{c}_j + R_j \mathbf{x})$, $u_1(\mathbf{x}) = W_j(\mathbf{c}_j + R_j \mathbf{x})$, $f_1(\mathbf{x}) = \nabla \cdot (\epsilon_1(\mathbf{x}) - 1) \nabla \Phi(\mathbf{c}_j + R_j \mathbf{x})$ and $\phi_1(\mathbf{x}) = h_j(\mathbf{c}_j + R_j \mathbf{x})$ where ϵ , W_j , Φ , h_j are as in Eqs (5.27)–(5.28).

From the discussion in Section 6.1, we know that there exists a unique harmonic function $\hat{u} \in H^1(B_1(\mathbf{0}))$, s.t.

$$\begin{cases} \Delta \hat{u}_1 = 0 & \text{in } B_1(\mathbf{0}), \\ \hat{u}_1 = \phi_1 & \text{on } \partial B_1(\mathbf{0}), \end{cases} \quad (6.34)$$

and \hat{u}_1 can be efficiently approximated by Eq. (6.32). Let $v = u_1 - \hat{u}_1 \in H_0^1(B_1(\mathbf{0}))$ and in consequence, v satisfies the following PDE

$$\begin{cases} -\nabla \cdot \epsilon_1 \nabla v = f & \text{in } B_1(\mathbf{0}), \\ v = 0 & \text{on } \partial B_1(\mathbf{0}), \end{cases} \quad (6.35)$$

where $f(\mathbf{x}) = \nabla \cdot (\epsilon_1(\mathbf{x}) - 1) \nabla \Phi(\mathbf{c}_j + R_j \mathbf{x}) + \nabla \cdot \epsilon_1(\mathbf{x}) \nabla \hat{u}_1(\mathbf{x})$.

Since the VdW-ball $B_{r_j}(\mathbf{c}_j) \subset \Omega_j$ and $\epsilon \equiv 1$ holds in $B_{r_j}(\mathbf{c}_j)$, we know that W_j defined in (5.27) is harmonic when restricted to the smaller ball $B_{r_j}(\mathbf{c}_j)$. In consequence, u_1 of Eq. (6.33) and v of Eq. (6.35) are both harmonic in $B_\delta(\mathbf{0})$, where δ is defined by

$$\delta = \frac{r_j}{r_j + r_0 + r_p} \in (0, 1).$$

Let $\mathcal{D} = B_1(\mathbf{0}) \setminus \overline{B_\delta(\mathbf{0})}$ represent the region between $\partial B_1(\mathbf{0})$ and $\partial B_\delta(\mathbf{0})$ and define the subspace $H_{0,\delta}^1(\mathcal{D})$ of the Sobolev space $H^1(\mathcal{D})$ as follows

$$H_{0,\delta}^1(\mathcal{D}) = \{w \in H^1(\mathcal{D}) : w|_{\partial B_1(\mathbf{0})} = 0\}.$$

In order to find the weak solution restricted to $H_{0,\delta}^1(\mathcal{D})$, we can write a variational formulation as: find $v \in H_{0,\delta}^1(\mathcal{D})$, s.t. $\forall w \in H_{0,\delta}^1(\mathcal{D})$,

$$\int_{\mathcal{D}} \epsilon_1 \nabla v \cdot \nabla w + \int_{\partial B_\delta(\mathbf{0})} (\mathcal{T}v) w = \int_{\mathcal{D}} f w, \quad (6.36)$$

where we use the fact that $\epsilon_1|_{\partial B_\delta(\mathbf{0})} = 1$. The operator \mathcal{T} is the Dirichlet-to-Neumann operator of the harmonic extension in $B_\delta(\mathbf{0})$, that in terms of spherical harmonics is given below. Assume that we have an expansion of the Dirichlet boundary condition $v|_{\partial B_\delta(\mathbf{0})}$ as follows

$$v|_{\partial B_\delta(\mathbf{0})}(\delta, \theta, \varphi) = \sum_{\ell=0}^{\infty} \sum_{m=-\ell}^{\ell} \alpha_{\ell m} Y_\ell^m(\theta, \varphi), \quad 0 \leq \theta \leq \pi, \quad 0 \leq \varphi < 2\pi. \quad (6.37)$$

Then, we can extend $v|_{\partial B_\delta(\mathbf{0})}$ harmonically from $\partial B_\delta(\mathbf{0})$ to the ball $B_\delta(\mathbf{0})$, i.e.,

$$v|_{B_\delta(\mathbf{0})}(r, \theta, \varphi) = \sum_{\ell=0}^{\infty} \sum_{m=-\ell}^{\ell} \alpha_{\ell m} \left(\frac{r}{\delta}\right)^\ell Y_\ell^m(\theta, \varphi), \quad 0 \leq r \leq \delta, \quad 0 \leq \theta \leq \pi, \quad 0 \leq \varphi < 2\pi. \quad (6.38)$$

Denote by \mathbf{n}_δ the unit normal vector on the sphere $\partial B_\delta(\mathbf{0})$ pointing outwards with respect to the ball $B_\delta(\mathbf{0})$. In consequence, we can compute $\partial_{\mathbf{n}_\delta} v = \nabla v \cdot \mathbf{n}_\delta$ consisting of the normal derivative of v on $\partial B_\delta(\mathbf{0})$:

$$\mathcal{T}v(\delta, \theta, \varphi) := \partial_{\mathbf{n}_\delta} v(\delta, \theta, \varphi) = \sum_{\ell=0}^{\infty} \sum_{m=-\ell}^{\ell} \alpha_{\ell m} \left(\frac{\ell}{\delta}\right) Y_\ell^m(\theta, \varphi), \quad 0 \leq \theta \leq \pi, \quad 0 \leq \varphi < 2\pi. \quad (6.39)$$

It is also easy to see that the bilinear form on the left side of the variational formulation (6.36) is symmetric and coercive due to properties of the Dirichlet-to-Neumann operator \mathcal{T} .

6.2.1 Galerkin Discretization

In order to find basis functions belonging to $H_{0,\delta}^1(\mathcal{D})$, we first introduce the radial functions

$$\varphi_i(r) = (1-r)L_i' \left(\frac{2(r-\delta)}{1-\delta} - 1 \right),$$

implying that $\varphi_i(1) = 0$. Here, L_i denotes the Legendre polynomial of i -th degree. We then discretize both, the radial part and the angular part of the unknown v , meaning that we represent v by linear combination of the basis functions $\{\varphi_i(r)Y_\ell^m(\theta, \varphi)\}$ with $1 \leq i \leq N$, $0 \leq \ell \leq \ell_{\max}$ and $-\ell \leq m \leq \ell$, where N denotes the maximum degree of Legendre polynomials and ℓ_{\max} denotes the maximum degree of spherical harmonics as in Section 6.1. The spanned space of these functions is denoted by $\mathcal{V}_{N,\ell_{\max}}(\mathcal{D})$ which is defined as follows

$$\mathcal{V}_{N,\ell_{\max}}(\mathcal{D}) = \text{span} \{\varphi_i(r)Y_\ell^m(\theta, \varphi) \mid 1 \leq i \leq N, 0 \leq \ell \leq \ell_{\max}, -\ell \leq m \leq \ell\} \subset H_{0,\delta}^1(\mathcal{D}).$$

Then, we consider a Galerkin discretization of the variational formulation (6.36) that reads: find $\tilde{v} \in \mathcal{V}_{N, \ell_{\max}}(\mathcal{D})$, such that

$$\forall \tilde{w} \in \mathcal{V}_{N, \ell_{\max}}(\mathcal{D}) : \quad \int_{\mathcal{D}} \epsilon_1 \nabla \tilde{v} \cdot \nabla \tilde{w} + \int_{\partial B_\delta(\mathbf{0})} (\mathcal{T} \tilde{v}) \tilde{w} = \int_{\mathcal{D}} f \tilde{w}. \quad (6.40)$$

Since $\tilde{v} \in \mathcal{V}_{N, \ell_{\max}}(\mathcal{D})$, we can write \tilde{v} in the form of

$$\tilde{v}(r, \theta, \varphi) = \sum_{i=0}^N \sum_{\ell=0}^{\ell_{\max}} \sum_{m=-\ell}^{\ell} v_{i\ell m} \varphi_i(r) Y_\ell^m(\theta, \varphi), \quad \forall \delta \leq r \leq 1, \quad 0 \leq \theta \leq \pi, \quad 0 \leq \varphi < 2\pi. \quad (6.41)$$

and we consequently have

$$\mathcal{T} \tilde{v}|_{B_\delta(\mathbf{0})}(\delta, \theta, \varphi) = \sum_{i=0}^N \sum_{\ell=0}^{\ell_{\max}} \sum_{m=-\ell}^{\ell} v_{i\ell m} \left(\frac{\ell}{\delta} \right) \varphi_i(\delta) Y_\ell^m(\theta, \varphi). \quad (6.42)$$

By substituting (6.41)–(6.42) into (6.40) and taking the test function $\tilde{w} \in \mathcal{V}_{N, \ell_{\max}}(\mathcal{D})$ as $\tilde{w} = \varphi_{i'}(r) Y_{\ell'}^{m'}(\theta, \varphi)$, we then obtain the a system of linear equations: $\forall 1 \leq i' \leq N, \quad 0 \leq \ell' \leq \ell_{\max}, \quad -\ell' \leq m' \leq \ell'$,

$$\sum_{i=0}^N \sum_{\ell=0}^{\ell_{\max}} \sum_{m=-\ell}^{\ell} v_{i\ell m} \left(\int_{\mathcal{D}} \epsilon_1 \nabla (\varphi_i Y_\ell^m) \cdot \nabla (\varphi_{i'} Y_{\ell'}^{m'}) + \frac{\ell}{\delta} \int_{\partial B_\delta(\mathbf{0})} \varphi_i Y_\ell^m \varphi_{i'} Y_{\ell'}^{m'} \right) = \int_{\mathcal{D}} f \varphi_{i'} Y_{\ell'}^{m'}. \quad (6.43)$$

In order to write the corresponding system of linear equations, we define an index

$$k = N(\ell^2 + m + \ell) + i \in \{1, 2, \dots, N(\ell_{\max} + 1)^2\}$$

which corresponds to the triple (i, ℓ, m) through a one-to-one mapping between k and (i, ℓ, m) . Assume that k corresponds to (i, ℓ, m) and k' corresponds to (i', ℓ', m') . Then, we can recast the set of equations (6.43) as a linear system of the form

$$\mathbf{A}X = F. \quad (6.44)$$

Here \mathbf{A} is a symmetric matrix of dimension $N(\ell_{\max} + 1)^2 \times N(\ell_{\max} + 1)^2$ with elements $(\mathbf{A})_{kk'}$, for all $1 \leq k, k' \leq N(\ell_{\max} + 1)^2$, defined by

$$(\mathbf{A})_{k'k} = \int_{\mathcal{D}} \epsilon_1 \nabla (\varphi_i Y_\ell^m) \cdot \nabla (\varphi_{i'} Y_{\ell'}^{m'}) + \frac{\ell}{\delta} \int_{\partial B_\delta(\mathbf{0})} \varphi_i Y_\ell^m \varphi_{i'} Y_{\ell'}^{m'}, \quad (6.45)$$

X is the column vector of $N(\ell_{\max} + 1)^2$ unknowns $v_{i\ell m}$, i.e.,

$$(X)_k = v_{i\ell m}, \quad \forall 1 \leq k \leq N(\ell_{\max} + 1)^2 \quad (6.46)$$

and F is also a column vector with $N(\ell_{\max} + 1)^2$ entities defined by

$$(F)_{k'} = \int_{\mathcal{D}} f \varphi_{i'} Y_{\ell'}^{m'}, \quad \forall 1 \leq k' \leq N(\ell_{\max} + 1)^2. \quad (6.47)$$

In summary, to solve Eq. (6.36), we finally need to solve the linear system (6.44) to obtain all coefficients $v_{i\ell m}$ and then obtain an approximate solution $\tilde{v}(r, \theta, \varphi) \in \mathcal{V}_{N, \ell_{\max}}(\mathcal{D})$ according to Eq. (6.41). Considering that v is harmonic in $B_\delta(\mathbf{0})$, \tilde{v} can then be extended harmonically in the ball $B_\delta(\mathbf{0})$ following (6.38). Therefore, we obtain an approximate solution defined on $B_1(\mathbf{0})$ to Eq. (6.35).

Remark 6.1. *In the global iterative procedure of Section 4.2, we compute the matrix \mathbf{A} of Eq. (6.44) for each subdomain Ω_j a priori, since each \mathbf{A} associated with Ω_j can be reused within the iterative GP-solver for solving Eq. (4.24) and for the outer iterations [1]–[4]. This helps to reduce considerably the cost of the global procedure at the cost of more memory requirements.*

6.2.2 Numerical integration

In order to implement the method, the integrals in Eq. (6.45) and Eq. (6.47) need to be further computed. We start by observing that the second term in Eq. (6.45) can be simplified

$$\frac{\ell}{\delta} \int_{\partial B_\delta(\mathbf{0})} \varphi_i Y_\ell^m \varphi_{i'} Y_{\ell'}^{m'} = \ell \delta \varphi_i(\delta) \varphi_{i'}(\delta) \int_{\mathbb{S}^2} Y_\ell^m Y_{\ell'}^{m'} = \ell \delta \varphi_i(\delta) \varphi_{i'}(\delta) \delta_{\ell\ell'} \delta_{mm'}, \quad (6.48)$$

where $\delta_{\ell\ell'}$ and $\delta_{mm'}$ are both the Kronecker deltas. In consequence, the solution matrix (\mathbf{A}) is symmetric. Next, we present the numerical integration over \mathcal{D} that is used to approximate the integral in the first term in Eq. (6.45) and the integral in Eq. (6.47).

The integral over \mathcal{D} can be divided into two parts: the radial part and spherical part, that is to say, for any given function $h \in L^1(B_1(\mathbf{0}))$, we can compute its integral over \mathcal{D} separately as below

$$\int_{\mathcal{D}} h(\mathbf{x}) d\mathbf{x} = \int_\delta^1 r^2 \int_{\mathbb{S}^2} h(r, \mathbf{s}) d\mathbf{s} dr, \quad (6.49)$$

where $\mathbf{s} \in \mathbb{S}^2$ and $\mathbf{x} = r\mathbf{s}$. To compute the spherical part of this integral, we use again the Lebedev quadrature rule for the unit sphere as in Section 6.1. To integrate the radial part numerically, we use the Legendre-Gauss-Lobatto (LGL) quadrature rule [22] defined by the integration points $x_m \in [-1, 1]$ and their weights w_m^{lgl} , $1 \leq m \leq N_{\text{lgl}}$, where N_{lgl} represents the number of LGL points. Using the change of variable $r = \frac{1-\delta}{2}(x+1) + \delta$, $x \in [-1, 1]$, we approximate the integral by the following quadrature rule

$$\begin{aligned} \int_{\mathcal{D}} h(\mathbf{x}) d\mathbf{x} &= \int_\delta^1 r^2 \int_{\mathbb{S}^2} h(r, \mathbf{s}) d\mathbf{s} dr \\ &= \int_{-1}^1 \frac{1-\delta}{2} \left(\frac{1-\delta}{2}(x+1) + \delta \right)^2 \int_{\mathbb{S}^2} h \left(\frac{1-\delta}{2}(x+1) + \delta, \mathbf{s} \right) d\mathbf{s} dx \\ &\approx \frac{1-\delta}{2} \sum_{m=1}^{N_{\text{lgl}}} \sum_{n=1}^{N_{\text{leb}}} w_m^{\text{lgl}} w_n^{\text{leb}} \left(\frac{1-\delta}{2}(x_m+1) + \delta \right)^2 h \left(\frac{1-\delta}{2}(x_m+1) + \delta, \mathbf{s}_n \right). \end{aligned} \quad (6.50)$$

The first integral of Eq. (6.45) and the integral of Eq. (6.47) can then be numerically computed using this quadrature.

7 Numerical results

In this section, we present some numerical results of the proposed method for solving the PDEs (4.13)–(4.14). Before investigating a realistic solute molecule, we will start to test the GP-solver for the unit sphere. We then consider small molecules and compute the electrostatic contribution to the solvation energy to study its dependency with respect to numerous parameters.

7.1 GP-solver for the unit sphere

We first test the GP-solver for solving Eq. (6.33) with a single sphere, as presented in Section 6.2. For the sake of simplicity, we assume here that the permittivity ϵ only depends on the radial variable r , i.e., the permittivity is symmetric. Let $r_1 = 0.4$, $r_p = 0.3$, $r_0 = 0.3$ and define the permittivity function $\epsilon(r)$ by

$$\epsilon(r) = \begin{cases} 1 & \text{if } 0 \leq r \leq r_1, \\ H\left(\frac{r-r_1}{r_p+r_0}\right) & \text{if } r_1 \leq r \leq 1, \\ \epsilon_s & \text{if } r \geq 1, \end{cases} \quad (7.51)$$

where H has been defined by Eq. (3.3) and $\epsilon_s = 10$. Assuming that the sphere carries a point charge 1 at its center, i.e., $q_1 = 1$, we take $\Phi = \frac{1}{r}$, $f_1 = -\frac{\epsilon'(r)}{r^2}$ and $\phi_1 = -1$ in Eq. (6.33). Since both, the permittivity function and the solution, only depend on the radius, the discretization of the angular part can be neglected, i.e., $\ell_{\max} = 0$. To have a good approximation in the radial direction, we set a high maximum degree of Legendre polynomials $N = 20$ and a large number of LGL points $N_{\text{lgl}} = 200$. By running the GP-solver, we then obtain Figure 5 illustrating the permittivity $\epsilon(r)$ and the (approximate) solution $u_1(r)$ to Eq. (6.33). It is observed that $u_1(r)$ is constant in $[0, 0.4]$ because of the harmonicity.

7.2 Electrostatic contribution to the solvation energy

With the domain decomposition method using the GP-solver for solving Eq. (4.24) and the dd-COSMO method for solving (4.25), we can then solve numerically Eqs (4.22)–(4.23) following the iterative procedure presented in Section 4.2.

To study the convergence of the proposed method with respect to the number of outer iterations, we first take the example of formaldehyde. The following discretization parameters are used: the maximum degree of spherical harmonics $\ell_{\max} = 11$, the number of Lebedev points $N_{\text{leb}} = 1202$, the maximum degree of Legendre polynomials $N = 15$, the number of LGL nodes $N_{\text{lgl}} = 50$. These parameters are given based on a further study in Section 7.6. Furthermore, we take the solvent permittivity $\epsilon_s = 78.4$ (water, at room temperature 25°C), the solvent probe radius $r_p = 1.5\text{\AA}$ and $r_0 = 1\text{\AA}$. Since the reaction potential usually has an order of magnitude of 10^{-3} , we use the convention that in the following content the stopping criterion is set to $\text{To1} = 10^{-7}$ by default, which is the tolerance for the increment of E^s between iterations. In addition, we use another convention that at each outer iteration of the global strategy, the number of inner iterations for solving the GP-equation (4.24) is fixed to be 8. This number is determined empirically and it allows to obtain an accurate enough numerical solution to Eq. (4.24) at each outer iteration. The error of the electrostatic contribution is computed as

$$\text{Error}(N_{\text{it}}) = |E_{N_{\text{it}}}^s - E_{\infty}^s|, \quad (7.52)$$

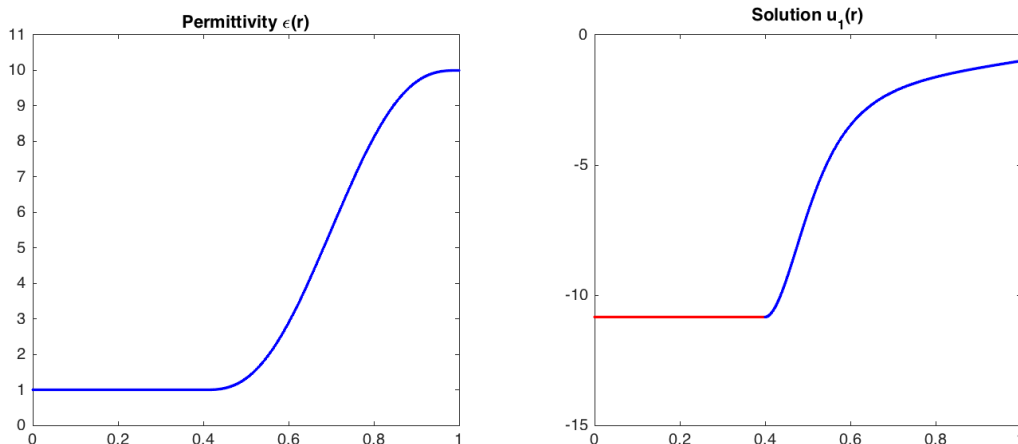


Figure 5: The left figure illustrates the dielectric permittivity $\epsilon(r)$; the right plots the solution $u_1(r)$ to Eq. (6.33). Only the blue part is subject to the computational domain, the red part of the curve depicts the harmonic extension.

where $E_{N_{it}}^s$ is the electrostatic contribution computed at the N_{it} -th outer iteration in Section 4.2 and the “exact” electrostatic contribution E_∞^s is obtained after 15 outer iterations (this number is large enough, see the left side of Figure 6) with the same discretization parameters as above-mentioned. In Figure 6, which illustrates the numerical electrostatic contribution to the solvation energy of formaldehyde with respect to the number of outer iterations N_{it} , it is observed that the error of electrostatic contribution converges geometrically with respect to N_{it} and the procedure stops at $N_{it} = 5$ when the stopping criterion is reached, i.e., $|E_{N_{it}}^s - E_{N_{it}-1}^s| < \text{Tol}$.

Then, we present the example of a larger molecule, the caffeine consisting of 24 atoms, with the parameters $\ell_{\max} = 9$, $N_{\text{leb}} = 350$, $N = 15$, $N_{\text{igl}} = 30$, $\epsilon_s = 78.4$, $r_p = 1.5\text{\AA}$, $r_0 = 1\text{\AA}$. The discretization parameters are taken smaller than those for formaldehyde because of the running time. This does not matter since we only want to study the convergence of the method with respect to the number of outer iterations. As above, the “exact” electrostatic contribution E_∞^s is obtained after 15 outer iterations and the error is computed from (7.52). As can be seen in Figure 7, the error of electrostatic contribution converges also geometrically with respect to N_{it} .

7.3 Graphical illustration of the reaction potential

We give here some graphical illustration of the reaction potential in the extended cavity Ω_0 and on the SES. In Figure 8, we illustrate the reaction potential W of hydrogen-fluoride and the magnitude of the corresponding reaction field (i.e., ∇W). In Figure 9 and 10, we illustrate the reaction potential of hydrogen-fluoride, formaldehyde and caffeine in water. The rotational symmetry of hydrogen-fluoride and the mirror symmetry of formaldehyde are observed as expected.

7.4 Thickness of the dielectric boundary layer

We then draw the attention to the influence of the thickness of dielectric boundary layer, which is given by $r_p + r_0$. For the sake of simplicity, we fix the parameter $r_0 = 0\text{\AA}$, implying that Γ_0 and

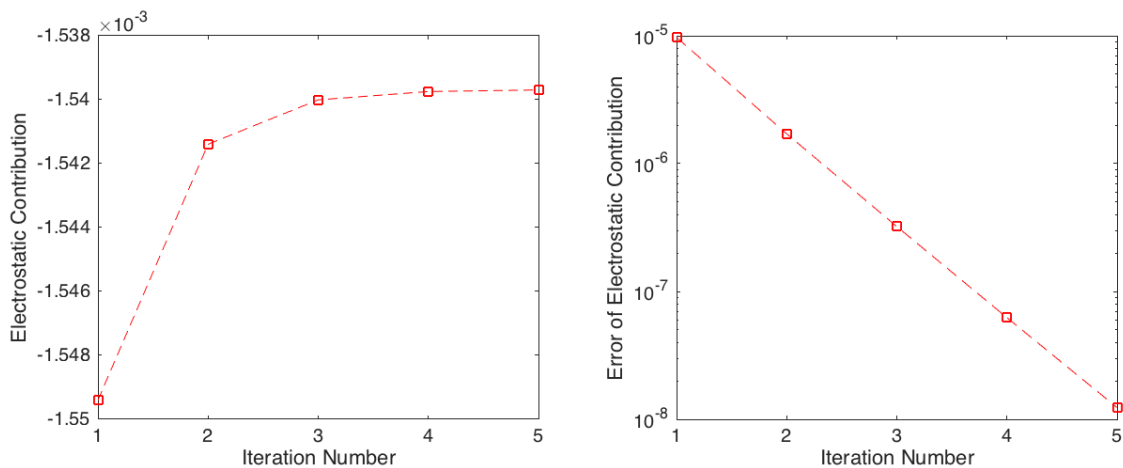


Figure 6: On the left, the curve illustrates the computed electrostatic contribution to the solvation energy of formaldehyde with respect to N_{it} ; on the right, the curve illustrates the error of the electrostatic contribution with respect to N_{it} . The following parameters are used: $\ell_{\max} = 11$, $N_{\text{leb}} = 1202$, $N = 15$, $N_{\text{gl}} = 50$, $\epsilon_s = 78.4$, $r_p = 1.5\text{\AA}$, $r_0 = 1\text{\AA}$.

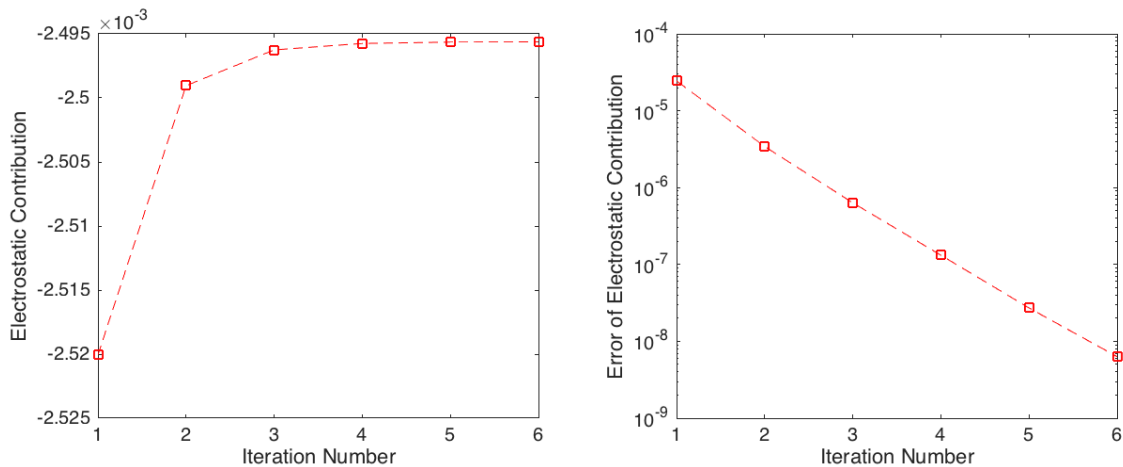


Figure 7: On the left, the curve illustrates the numerical electrostatic contribution to the solvation energy of caffeine with respect to N_{it} ; on the right, the curve illustrates the error of the electrostatic contribution with respect to N_{it} . The following parameters are used: $\ell_{\max} = 9$, $N_{\text{leb}} = 350$, $N = 15$, $N_{\text{gl}} = 30$, $\epsilon_s = 78.4$, $r_p = 1.5\text{\AA}$, $r_0 = 1\text{\AA}$.

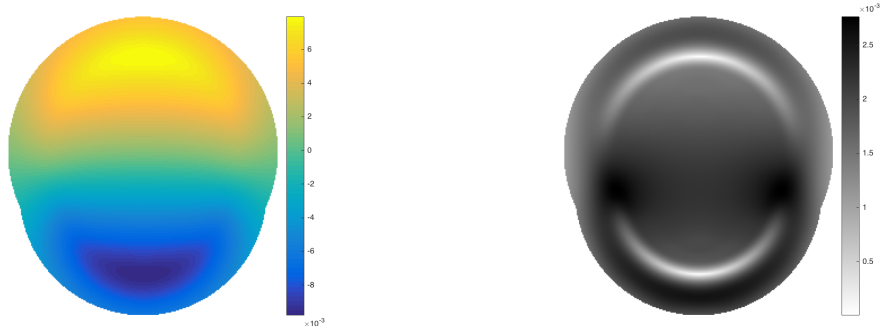


Figure 8: The reaction potential (left) and the magnitude of the corresponding reaction field (right) in the YZ-plane for the hydrogen-fluoride molecule with two atoms, with the parameters $\ell_{\max} = 11$, $N_{\text{leb}} = 1202$, $N = 15$, $N_{\text{igl}} = 50$, $\epsilon_s = 2$, $r_p = 1.5\text{\AA}$, $r_0 = 1\text{\AA}$. The colorbars represent respectively the reaction potential value and the magnitude of the reaction field.

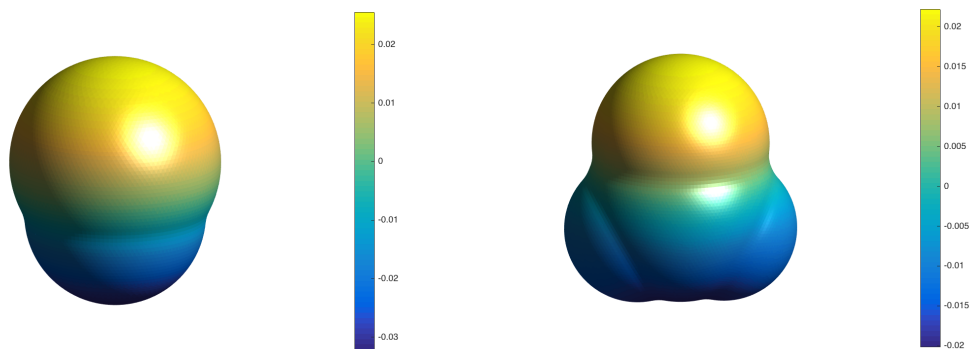


Figure 9: Reaction potential of hydrogen-fluoride and formaldehyde on the SES, both computed with the parameters $\ell_{\max} = 11$, $N_{\text{leb}} = 1202$, $N = 15$, $N_{\text{igl}} = 50$, $\epsilon_s = 78.4$, $r_p = 1.5\text{\AA}$, $r_0 = 1\text{\AA}$.

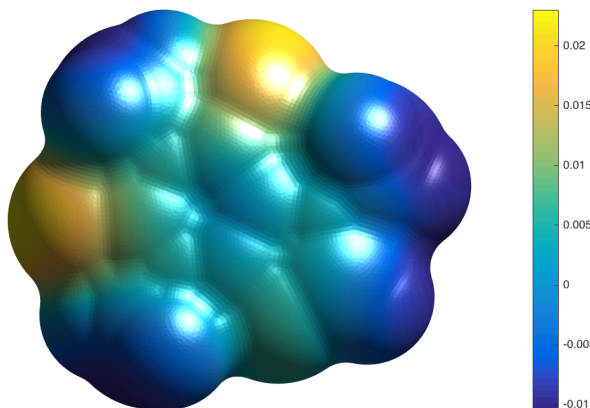


Figure 10: Reaction potential of caffeine on the SES, computed with the parameters $\ell_{\max} = 9$, $N_{\text{leb}} = 350$, $N = 15$, $N_{\text{igl}} = 30$, $\epsilon_s = 78.4$, $r_p = 1.5\text{\AA}$, $r_0 = 1\text{\AA}$.

Γ_{sas} coincide. In the ddPCM algorithm presented in [31], the permittivity is discontinuous across the dielectric boundary and jumps from 1 to ϵ_s . In the following test, we take Γ_0 as the dielectric boundary in the ddPCM algorithm and expect that the numerical electrostatic contribution to the solvation energy computed from our method tends to the one computed from the ddPCM algorithm as the thickness of dielectric boundary layer tends to zero, i.e., $r_p \rightarrow 0$. This implies that both, Γ_{ses} and Γ_0 , tend to the VdW-surface.

To verify this, we take again the example of hydrogen-fluoride. Figure 11 illustrates the numerical electrostatic contribution to the solvation energy with respect to n where the thickness of dielectric boundary layer is parametrized by $r_p = 2^{-n}\text{\AA}$. We observe that the electrostatic contributions from both algorithms almost tend to coincide when the layer vanishes. This means that the proposed method is consistent with the ddPCM in this case.

7.5 Solvent dielectric constant

We illustrate in Figure 12 how the electrostatic contribution to the solvation energy and the total number of outer iterations varies with respect to different solvent permittivities $\epsilon_s = 2^k$, $k = 1, 2, \dots, 15$. We observe that the numerical electrostatic contribution to the solvation energy varies smoothly and converges to some quantity for increasing solvent permittivities ϵ_s . Another interesting observation is that when ϵ_s becomes large, the total number of outer iterations tends to decrease. This can be explained by the fact that the solvent is conductor-like and consequently, the initial guess of potential g^0 is very accurate for high permittivities ϵ_s .

7.6 Discretization parameters

We consider the dichloromethane solvent ($\epsilon_s = 8.93$) at room temperature 25°C . First of all, we compute numerically the “exact” electrostatic contribution to the solvation energy of hydrogen-fluoride, denoted by E_{exact}^s , with large discretization parameters $\ell_{\max} = 20$, $N_{\text{leb}} = 4334$, $N =$

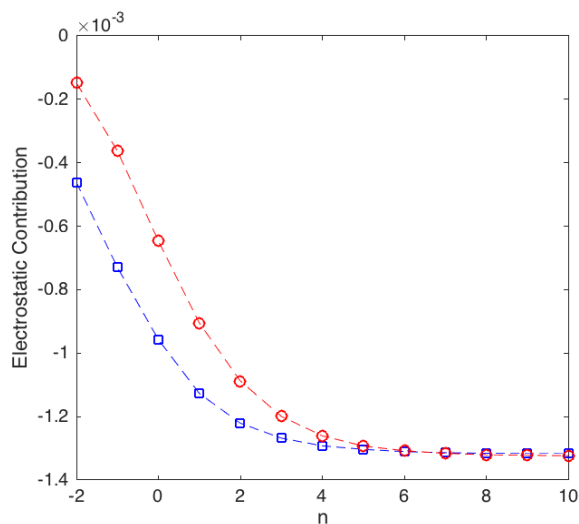


Figure 11: The blue curve plots the electrostatic contribution of hydrogen-fluoride with respect to n (the layer thickness 2^{-n}\AA), computed from the proposed algorithm with the parameters $\ell_{\max} = 11$, $N_{\text{leb}} = 1202$, $N = 15$, $N_{\text{igl}} = 50$, $\epsilon_s = 2$; the red curve plots the results computed from the ddPCM algorithm with the same parameters of spherical harmonics $\ell_{\max} = 11$, $N_{\text{leb}} = 1202$ and the same solvent permittivity $\epsilon_s = 2$.

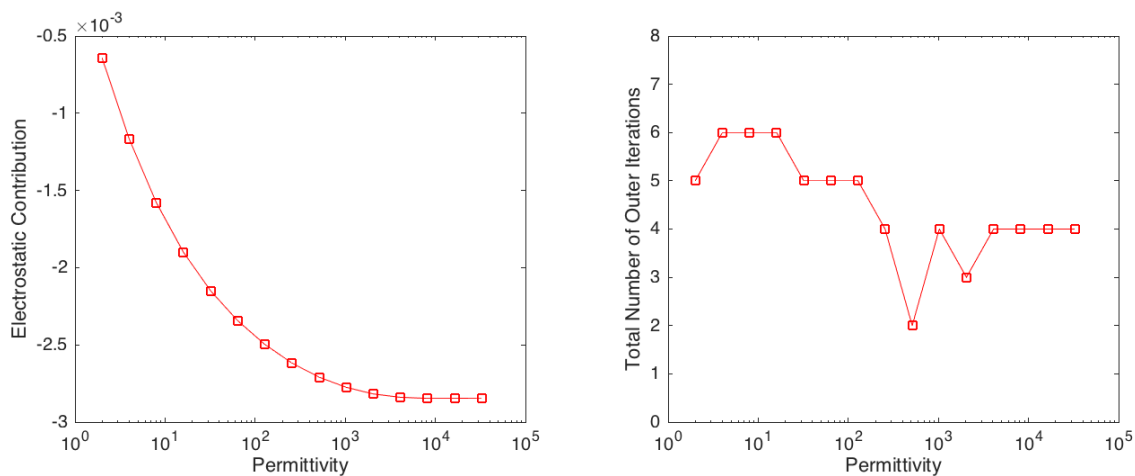


Figure 12: The left figure shows the electrostatic contribution to the solvation energy of hydrogen-fluoride when the solvent dielectric permittivity ϵ_s increases; the right figure plots the total number of outer iterations to reach the stopping criterion To1 with respect to ϵ_s . The following parameters are used: $\ell_{\max} = 11$, $N_{\text{leb}} = 1202$, $N = 20$, $N_{\text{igl}} = 50$, $r_p = 1.5\text{\AA}$, $r_0 = 1\text{\AA}$.

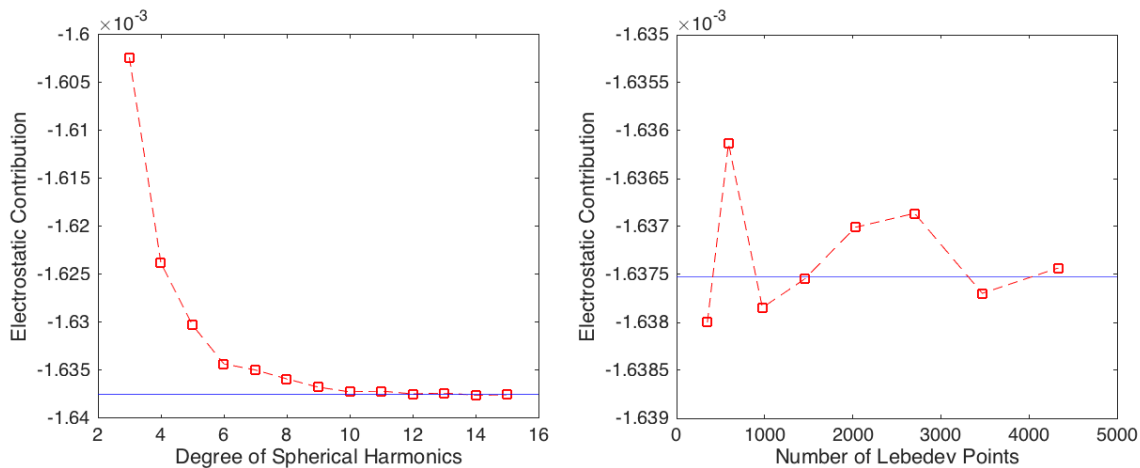


Figure 13: The left figure plots the electrostatic contribution to the solvation energy of hydrogen-fluoride with respect to ℓ_{\max} when N_{leb} is set to 1454. The right figure plots the electrostatic contribution with respect to N_{leb} when ℓ_{\max} is set to 15. In both figures, the blue line represents the “exact” electrostatic contribution E_{exact}^s . In addition, the following parameters are used: $N = 20$, $N_{\text{lgl}} = 50$, $\epsilon_s = 8.93$, $r_p = 1.5\text{\AA}$, $r_0 = 1\text{\AA}$.

25, $N_{\text{lgl}} = 50$ and the parameters of the dielectric boundary layer set to $r_p = 1.5\text{\AA}$, $r_0 = 1\text{\AA}$. We treat E_{exact}^s as the benchmark of the electrostatic contribution to the solvation energy.

We then illustrate how the electrostatic contribution to the solvation energy of hydrogen-fluoride varies respectively with respect to the maximum degree ℓ_{\max} of spherical harmonics and to the number N_{leb} of Lebedev points in the dichloromethane solvent. On the left of Figure 13, we report the electrostatic contribution with respect to ℓ_{\max} which varies from 3 to 15. Further, on the right of Figure 13, we report the electrostatic contribution with respect to N_{leb} which varies from 350 to 4334. From the left figure, we observe that the proposed algorithm provides systematically improvable approximations when the parameters of spherical harmonics increases.

Similarly as above, we now illustrate how the electrostatic contribution to the solvation energy of hydrogen-fluoride varies with respect to the maximum degree N of Legendre polynomials and to the number N_{lgl} of LGL points in the dichloromethane solvent. On the left of Figure 14, we report the electrostatic contribution with respect to N varying from 6 to 20. Further, on the right of Figure 14, we report the electrostatic contribution with respect to N_{lgl} varying from 20 to 80. Again, it is observed that the proposed algorithm provides asymptotically systematically improvable approximations when the discretization of Legendre polynomials increases. These results help us to get a know-how in order to select, for a given molecule, the proper choice of discretization parameters ℓ_{\max} , N_{leb} , N , N_{lgl} for an acceptable accuracy.

7.7 Robustness with respect to geometrical parameters

We now study in Figure 15 the variation of the electrostatic contribution to the solvation energy of hydrogen-fluoride while rotating the fluoride atom around the hydrogen atom. We observe that the variation in the electrostatic contribution, which should be invariant with respect to the rotation

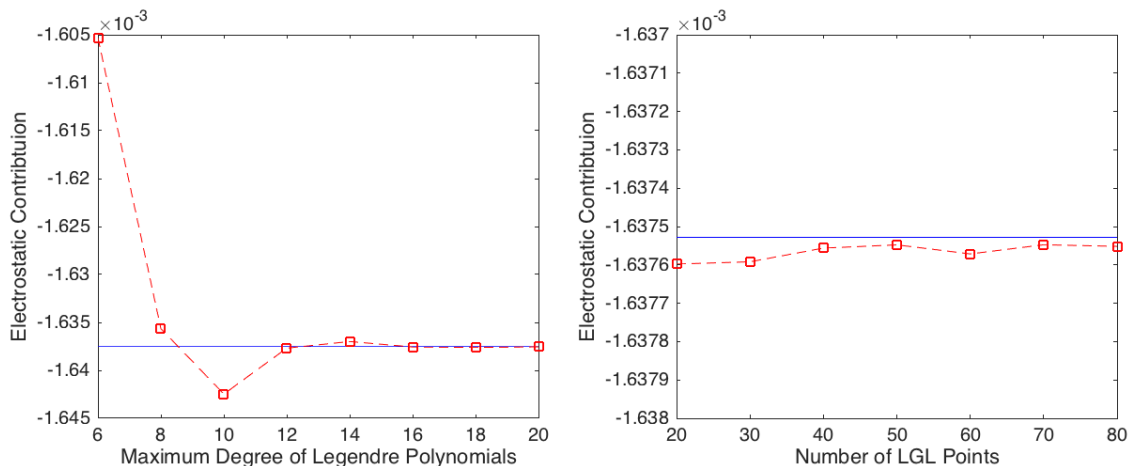


Figure 14: The left figure plots the electrostatic contribution to the solvation energy of hydrogen-fluoride with respect to N when N_{lgl} is set to 50. The right figure plots the electrostatic contribution with respect to N_{lgl} when N is set to 20. In both figures, the blue line represents the “exact” electrostatic contribution E_{exact}^s . In addition, the following parameters are used: $\ell_{\text{max}} = 15$, $N_{\text{leb}} = 1454$, $\epsilon_s = 8.93$, $r_p = 1.5\text{\AA}$, $r_0 = 1\text{\AA}$.

angle, is systematically controlled. For the two sets of parameters, see the caption of Figure 15, the variation is around 1.5% and 0.25% respectively.

Further, we study the electrostatic contribution to the solvation energy under a dissociation of hydrogen-fluoride. We vary the separation distance between the hydrogen atom and the fluoride atom from 8.96\AA to 9.36\AA where the topology of the SES changes in the sense that the SES becomes two disconnected subsurfaces, see Figure 16 for a geometrical illustration. The left plot of Figure 17 illustrates that the energy profile is completely smooth when the topology of the SES changes. The right figure of Figure 17 provides the electrostatic contribution to the solvation energy when the separation distance varies in a wider range from 1.77\AA to 9.37\AA .

We next study the smoothness of the numerical electrostatic contribution to the solvation energy of formaldehyde with respect to a topological change in the sense that the nature of the patches of the SES changes. We choose the coordinate system so that all nuclei lie in the yz -plane and that carbon and oxygen atoms have $y = 0$ coordinate. We then move the z -coordinate of the two hydrogen atoms further away from the carbon and oxygen atoms, see Figure 18 for an illustration. Figure 19 plots the numerical electrostatic contribution to the solvation energy with respect to the downwards displacement of the two hydrogen atoms. On the left, we plot the numerical electrostatic contribution with respect to displacement of the two hydrogen atoms in a large range from 0\AA to 1\AA . On the right, we plot the numerical electrostatic contribution in the neighborhood of the threshold when the concave SES patches, marked in blue in Figure 18, first appear and we observe that the energy-profile is approximately smooth.

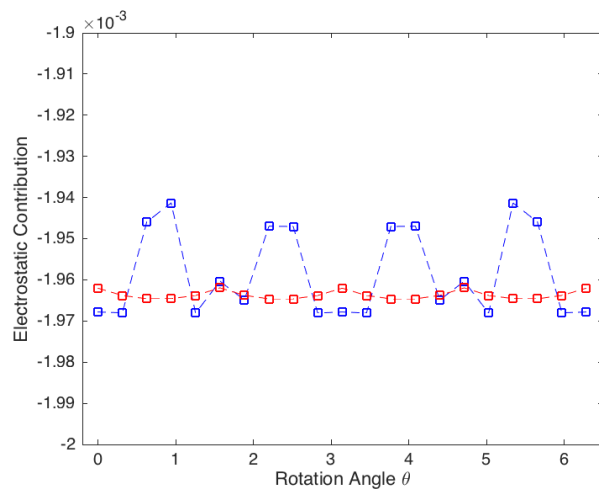


Figure 15: The variation of the electrostatic contribution to the solvation energy of hydrogen-fluoride with respect to the angle of rotating the fluoride atom around the hydrogen atom. The blue curve corresponds to the parameters $\ell_{\max} = 7$, $N_{\text{leb}} = 86$, $N = 10$, $N_{\text{igl}} = 20$, the red curve corresponds to the parameters $\ell_{\max} = 11$, $N_{\text{leb}} = 1202$, $N = 20$, $N_{\text{igl}} = 40$. Furthermore, the following parameters are used: $\epsilon_s = 8.93$, $r_p = 1.5\text{\AA}$, $r_0 = 1\text{\AA}$.

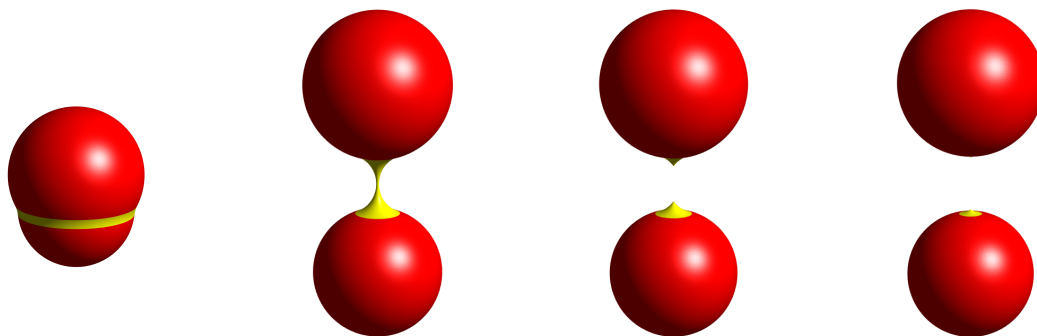


Figure 16: Topological change of the SES of hydrogen-fluoride when the distance between the two atomic centers increases. The most left figure illustrates the SES of hydrogen-fluoride in equilibrium and the three figures from the left to right corresponds to the distances between the centers increased respectively to 8.96\AA , 9.16\AA and 9.36\AA .

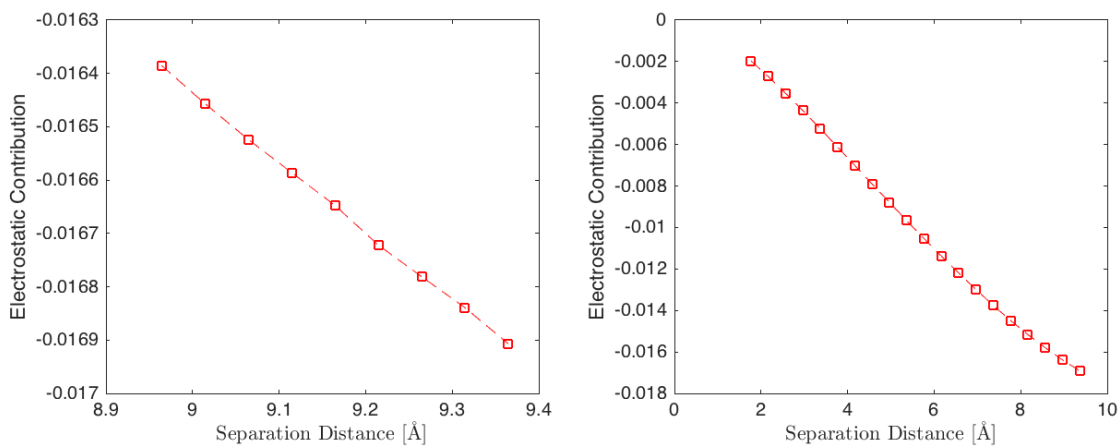


Figure 17: Electrostatic contribution of hydrogen-fluoride with respect to the separation distance between the atomic centers with parameters $\ell_{\max} = 11$, $N_{\text{leb}} = 1202$, $N = 20$, $N_{\text{igl}} = 40$, $\epsilon_s = 8.93$, $r_p = 1.5\text{\AA}$, $r_0 = 0\text{\AA}$. On the left, the separation distance varies between 8.96\AA and 9.36\AA where the topology of the SES changes as showed in Figure 16. On the right, the separation distance varies in a larger range.

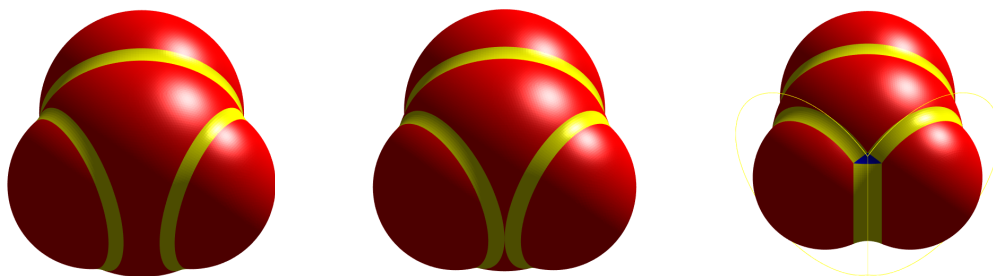


Figure 18: Different SESs of formaldehyde when the two hydrogen atoms displace downwards. The left figure illustrates the SES of formaldehyde in equilibrium; the middle figure illustrates the SES when concave patches are about to appear; the right figure illustrates the SES when the concave patches (in blue) have appeared.

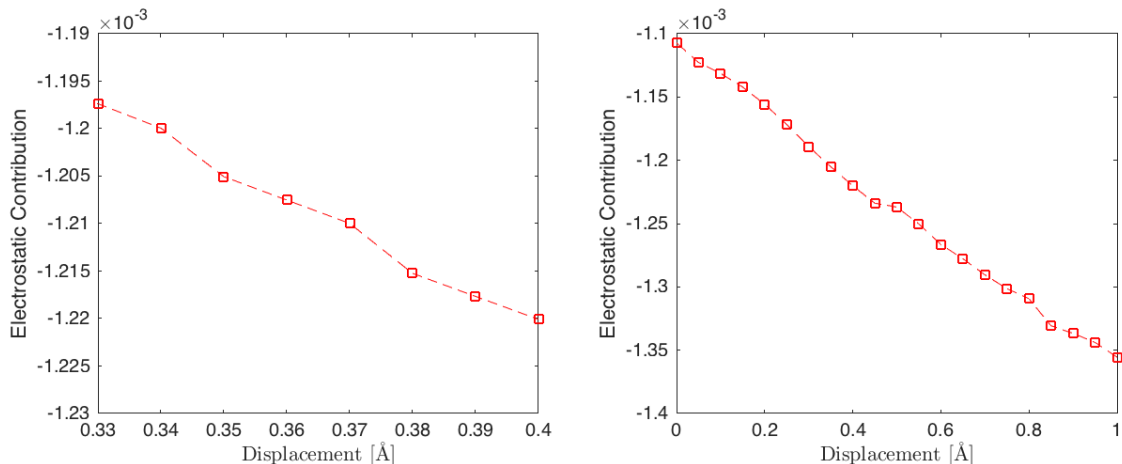


Figure 19: Electrostatic contribution to the solvation energy of formaldehyde with respect to the displacement of the two hydrogen atoms with parameters $\ell_{\max} = 11$, $N_{\text{leb}} = 1454$, $N = 15$, $N_{\text{igl}} = 50$, $\epsilon_s = 8.93$, $r_p = 1.5\text{\AA}$, $r_0 = 1\text{\AA}$. On the left, the displacement varies near the threshold when the concave SES patches first appear as showed in the middle of Figure 18. On the right, the displacement varies from 0\AA to 1\AA .

8 Conclusion

We have proposed a new Polarizable Continuum Model (PCM) based on the Solvent Excluded Surface cavity (SES-cavity). We introduced a switching region for the solute-solvent dielectric boundary based on the signed distance function to the SAS where the dielectric constant smoothly varies between one (vacuum) and ϵ_s (the solvent). This layer potentially also allows to describe local effects such as layers close to the solute-solvent interface. Further, to compute the electrostatic contribution to the solvation energy numerically, we lay out a mathematical framework to compute the solution on an unbounded domain that only involves to compute problems in a bounded domain (extended cavity). For each problem in the extended cavity, we propose to use Schwarz’s domain decomposition method where the global problem defined in the solute cavity is divided into simple sub-problems each defined in a ball. We provided numerical tests to illustrate the resulting energy profile is smooth with respect to geometrical parameters and that the energy is systematically improvable.

We focused here on the modeling part and the resulting discretization method. This work is meant to study the feasibility to propose a SES-based solvation model using a domain decomposition method and analyzing its properties. An upcoming paper will focus on an efficient implementation which is work in progress.

9 Acknowledgement

The authors would like to thank Pacal Frey, Eric Cancès, Filippo Lipparini and Benedetta Mennucci for the fruitful discussion about meshing molecular surfaces and constructing the new polarizable

continuum model. C. QUAN would like to acknowledge the support from the Fondation Sciences Mathématiques de Paris.

References

- [1] Basilevsky, M. V., Grigoriev, F. V., Nikitina, E. A., and Leszczynski, J. (2010). Implicit electrostatic solvent model with continuous dielectric permittivity function. *The Journal of Physical Chemistry B*, 114(7):2457–2466.
- [2] Cammi, R. and Mennucci, B. (2007). *Continuum Solvation Models in Chemical Physics: From Theory to Applications*. John Wiley.
- [3] Cancès, E., Maday, Y., and Stamm, B. (2013). Domain decomposition for implicit solvation models. *The Journal of chemical physics*, 139(5):054111.
- [4] Cancès, E. and Mennucci, B. (1998). New applications of integral equations methods for solvation continuum models: ionic solutions and liquid crystals. *Journal of mathematical chemistry*, 23(3-4):309–326.
- [5] Cancès, E., Mennucci, B., and Tomasi, J. (1997). A new integral equation formalism for the polarizable continuum model: Theoretical background and applications to isotropic and anisotropic dielectrics. *The Journal of chemical physics*, 107(8):3032–3041.
- [6] D’Abramo, M., D’Alessandro, M., Di Nola, A., Roccatano, D., and Amadei, A. (2005). Characterization of liquid behaviour by means of local density fluctuations. *Journal of molecular liquids*, 117(1):17–21.
- [7] Frisch, A. (2005). *Gaussian 03. U. User’s reference: manual version 7.1 (corresponding to Gaussian 03 revision D. 1)*. Gaussian.
- [8] Grant, J. A., Pickup, B. T., and Nicholls, A. (2001). A smooth permittivity function for Poisson–Boltzmann solvation methods. *Journal of computational chemistry*, 22(6):608–640.
- [9] Hackbusch, W. (2012). *Integral equations: theory and numerical treatment*, volume 120. Birkhäuser.
- [10] Haxton, D. J. (2007). Lebedev discrete variable representation. *Journal of Physics B: Atomic, Molecular and Optical Physics*, 40(23):4443.
- [11] Hirata, F. (2003). *Molecular theory of solvation*, volume 24. Springer Science & Business Media.
- [12] Im, W., Beglov, D., and Roux, B. (1998). Continuum solvation model: computation of electrostatic forces from numerical solutions to the Poisson–Boltzmann equation. *Computer Physics Communications*, 111(1):59–75.
- [13] Klamt, A. and Schüürmann, G. (1993). Cosmo: a new approach to dielectric screening in solvents with explicit expressions for the screening energy and its gradient. *Journal of the Chemical Society, Perkin Transactions 2*, (5):799–805.

- [14] Lee, B. and Richards, F. M. (1971). The interpretation of protein structures: estimation of static accessibility. *Journal of molecular biology*, 55(3):379–IN4.
- [15] Lipparini, F., Lagardère, L., Scalmani, G., Stamm, B., Cancès, E., Maday, Y., Piquemal, J.-P., Frisch, M. J., and Mennucci, B. (2014a). Quantum calculations in solution for large to very large molecules: A new linear scaling QM/continuum approach. *The journal of physical chemistry letters*, 5(6):953–958.
- [16] Lipparini, F., Lagardère, L., Stamm, B., Cancès, E., Maday, Y., Piquemal, J.-P., and Mennucci, B. (2015). ddCOSMO & ddPCM. <https://www.ddpcm.org>.
- [17] Lipparini, F., Scalmani, G., Lagardère, L., Stamm, B., Cancès, E., Maday, Y., Piquemal, J.-P., Frisch, M. J., and Mennucci, B. (2014b). Quantum, classical, and hybrid QM/MM calculations in solution: General implementation of the ddcosmo linear scaling strategy. *The Journal of chemical physics*, 141(18):184108.
- [18] Lipparini, F., Stamm, B., Cancès, E., Maday, Y., and Mennucci, B. (2013). Fast domain decomposition algorithm for continuum solvation models: Energy and first derivatives. *Journal of Chemical Theory and Computation*, 9(8):3637–3648.
- [19] Mennucci, B. (2010). Continuum solvation models: What else can we learn from them? *The Journal of Physical Chemistry Letters*, 1(10):1666–1674.
- [20] Mennucci, B., Cancès, E., and Tomasi, J. (1997). Evaluation of solvent effects in isotropic and anisotropic dielectrics and in ionic solutions with a unified integral equation method: theoretical bases, computational implementation, and numerical applications. *The Journal of Physical Chemistry B*, 101(49):10506–10517.
- [21] Nina, M., Beglov, D., and Roux, B. (1997). Atomic radii for continuum electrostatics calculations based on molecular dynamics free energy simulations. *The Journal of Physical Chemistry B*, 101(26):5239–5248.
- [22] Parter, S. V. (1999). On the Legendre–Gauss–Lobatto points and weights. *Journal of scientific computing*, 14(4):347–355.
- [23] Provorse, M. R., Peev, T., Xiong, C., and Isborn, C. M. (2016). Convergence of excitation energies in mixed quantum and classical solvent: Comparison of continuum and point charge models. *The Journal of Physical Chemistry B*, 120(47):12148–12159.
- [24] Quan, C. and Stamm, B. (2016). Mathematical analysis and calculation of molecular surfaces. *Journal of Computational Physics*, 322:760 – 782.
- [25] Quan, C. and Stamm, B. (2017). Meshing molecular surfaces based on analytical implicit representation. *Journal of Molecular Graphics and Modelling*, 71:200–210.
- [26] Quarteroni, A. and Valli, A. (1999). *Domain decomposition methods for partial differential equations*. Number CMCS-BOOK-2009-019. Oxford University Press.
- [27] Rappè, A. K., Casewit, C. J., Colwell, K., Goddard Iii, W., and Skiff, W. (1992). Uff, a full periodic table force field for molecular mechanics and molecular dynamics simulations. *Journal of the American Chemical Society*, 114(25):10024–10035.

- [28] Raschke, T. M., Tsai, J., and Levitt, M. (2001). Quantification of the hydrophobic interaction by simulations of the aggregation of small hydrophobic solutes in water. *Proceedings of the National Academy of Sciences*, 98(11):5965–5969.
- [29] Richards, F. M. (1977). Areas, volumes, packing and protein structure. *Annual Review of Biophysics and Bioengineering*, 6:151–176.
- [30] Sauter, S. A. and Schwab, C. (2010). Boundary element methods. In *Boundary Element Methods*, pages 183–287. Springer.
- [31] Stamm, B., Cancès, E., Lipparini, F., and Maday, Y. (2016). A new discretization for the polarizable continuum model within the domain decomposition paradigm. *The Journal of Chemical Physics*, 144(5):054101.
- [32] Tomasi, J., Mennucci, B., and Cammi, R. (2005). Quantum mechanical continuum solvation models. *Chemical reviews*, 105(8):2999–3094.
- [33] Tomasi, J. and Persico, M. (1994). Molecular interactions in solution: An overview of methods based on continuous distributions of the solvent. *Chemical Reviews*, 94(7):2027–2094.